Flexural rigidity of hawkmoth antennae depends on the bending direction

Adam Puchalski[1], Zoë McCarthy[1], Alexandre Varaschin Palaoro[1], Arthur A. Salamatin[1], Agnes Nagy-Mehesz[2], Guzeliya Korneva[2], Charles E. Beard[3], Jeffery Owens[4], Peter H. Adler[3] and Konstantin G. Kornev[1]

[1]Department of Materials Science and Engineering, Clemson University, Clemson, South Carolina, USA, 29634. E-mail: kkornev@clemson.edu

[2]Department of Bioengineering, Clemson University, Clemson, South Carolina USA, 29634

[3]Department of Plant and Environmental Sciences, Clemson University, Clemson, South Carolina USA, 29634

[4]Air Force Civil Engineer Center, Tyndall Air Force Base, Florida

Abstract

To probe its environment, the flying insect controllably flexes, twists, and maneuvers its antennae by coupling mechanical deformations with the sensory output. We question how the materials properties of insect antennae could influence their performance. A comparative study was conducted on four hawkmoth species: *Manduca sexta, Ceratomia catalpae, Manduca quinquemaculata,* and *Xylophanes tersa*. The morphology of the antennae of three hawkmoths that hover while feeding and one putatively non-nectar-feeding hawkmoth (*Ceratomia catalpa*) do not fundamentally differ, and all the antennae are comb-like (i.e., pectinate), markedly in males but weakly in females. Applying different weights to the free end of extracted cantilevered antennae, we discovered anisotropy in flexural rigidity when the antenna is forced to bend dorsally versus ventrally. The flexural rigidity of male antennae was less than that of females. Compared with the hawkmoths that hover while feeding, *Ceratomia catalpae* has almost two orders of magnitude lower flexural rigidity. Tensile tests showed that the stiffness of male and female antennae is almost the same. Therefore, the differences in flexural rigidity are explained by the distinct shapes of the antennal pectination. Like bristles in a comb, the pectinations provide extra rigidity to the antenna. We discuss the biological implications of these discoveries in relation to the flight habits of hawkmoths. Flexural anisotropy of antennae is expected in other groups of insects, but the targeted outcome may differ. Our work offers promising new applications of shaped fibers as mechanical sensors.

1. Introduction

Over millions of years of evolutionary history[1], insects developed unique fiber-based devices—antennae—with built-in sensing, actuation, and analytical neural circuitry[2, 3] allowing them to distinguish and decipher scents when searching for food or mates[2, 4-10], avoid obstacles [11], detect air movements, and control flight[12-17]. Although olfactory behavior and mechanisms of interactions of chemicals with the antennal sensilla and neural circuits have been intensively studied [2, 4-8, 18-21], the effect of antennal positioning and active odor sampling has only recently been recognized as an important behavioral feature [8, 22, 23].

The focus of previous studies has been mostly on the neuromechanics of olfaction where different types of sensilla are the most important mediators coupling air flow and neural circuitry[24, 25]. Flying insects, however, engage the entire antenna for mechanical sensing of the environment. Experiments on antennal removal have become popular since the classic studies by Johnson [26] in which bean aphid antennae, or parts of them, were amputated and replaced with artificial antennae. Without antennae, the insect could not maintain flight or prevent crashing with an obstacle. This conclusion was confirmed for locusts, cockroaches, hawkmoths, dragonflies, and true flies[12, 13, 17, 26, 27], suggesting the importance of the antennal beam for insect survival.

Despite the importance of antennal flexibility [11-13, 24, 25, 28-30], the difference between antennal behavior as a rigid rod or as a flexible beam is not fully appreciated in flight neuromechanics[15, 25]. The rigid-rod model carries information about antennal direction with respect to body direction [8, 15, 22, 23]. Within this model, the flying insect is assumed to sense the torque exerted by the wind on the two basal segments of the antenna, the pedicel–scape pair. For insects with short, stiff antennae much smaller than the insect body and forewing length, this model could be sufficient to serve as the mechanical input for neuromechanical models of environment sensing. The rigid-rod model, however, falls short when the antennae are long and flexible, like those in hawkmoths. For these insects, the rigid-rod model may oversimplify sensory cues because the torque on the pedicel–scape pair significantly depends on the entire antennal profile. The insect probably analyzes prior information on the profiles of the bent and twisted antennae under the wind load and rapidly relates it to the antennal profile at a given moment in time. Only by integrating this information would the insect be able to evaluate the strength and

direction of the wind and make decisions on how and where to maneuver to maintain stable flight [13, 17].

We investigate whether hawkmoths (family Sphingidae) could use specific morphological properties of their antennae to probe the wind direction, not at the level of a single sensillum but at the scale of the entire organism. At this scale, the antenna works as a mechanical beam and hence its inherent bending properties become critical [31]. We conducted a comparative analysis of the antennae of four hawkmoths (*Manduca sexta, Ceratomia catalpae, Manduca quinquemaculata,* and *Xylophanes tersa*) and related the morphology to flexural properties. The morphology of hawkmoth antennae is unique and differs between males and females[32-35]. *Ceratomia catalpae* can fly but has a short proboscis and putatively does not feed on floral nectar as adults. The three other hawkmoths have long proboscises and vigorously hover during feeding.

2. Materials and Methods

2.1 Studied species and measurements

We studied four hawkmoth species: *Manduca sexta* (n = 13), *Ceratomia catalpae* (n = 4)*, Manduca quinquemaculata* (n = 3), and *Xylophanes tersa* (n = 3). *Manduca sexta* and *C. catalpae* were reared in the laboratory, following our standard procedures[36]. We captured the two other hawkmoths, *M. quinquemaculata* and *X. tersa*, using an aerial hand net in the South Carolina Botanical Garden (Clemson University) from August to October 2022.

To measure the length and width of the antennae along with forewing length (a proxy for the size of the moth), we photographed dried, spread individuals in the Clemson University Arthropod Collection (CUAC). We imaged individual antennae, using a Canon EOS 7D camera with a Canon MP-E 65-mm lens and Helicon Remote version 3.9.7W. The length of the antenna was measured from the base of the scape to the tip of the terminal flagellomere. We used the 'segmented line' in Fiji-ImageJ to measure antennae because it allowed us to evaluate not only straight, but also curved structures (e.g., Fig. 2 f-m). We also divided the antenna into 5 sections: "base", "base-mid", "mid", "mid-tip", and "tip" to represent five distances along the length. In each of these sections, we measured the width of the dorsal side. These measurements allowed us to infer the shape of the antenna along its entire length. We also measured forewing length as the distance from the base of the forewing to its tip. We photographed at least 5 individuals of each

sex, except for *C. catalpae* females (n = 2) (total N = 37 individuals). We performed all measurements in Fiji-ImageJ.

2.2 Scanning Electron Microscopy (SEM)

After experiments, the antennae were prepared for SEM. They were placed in a centrifuge tube (VWR) with a damp piece of toweling to maintain moisture. On the day of imaging, samples were placed in liquid nitrogen and then cut into cross sections. The cross sections were mounted on an SEM stub with carbon-graphite adhesive tape. A Hitachi SU5000 VP-SEM was used, with the BSE detector at an accelerating voltage of 15 kV or 20 kV in low-vacuum mode at 50 Pa.

2.3. Histology

After taking the live insect from the refrigerator, antennae were cut with scissors and fixed in 10% neutral buffered formalin at room temperature for 3 days and prepared in a tissue processor for paraffin embedding. Sections 5–7 μm thick were cut with a Leica RM2255 microtome and mounted on slides. The sections were deparaffinized, rehydrated, and stained with H&E (hematoxylin and eosin), according to the manufacturer's (Newcomers Supply, WI) instructions. Images were captured using a Keyence BZ-X810 All-in-one inverted microscope.

2.4. Bending Test

We used microscissors to cut the antennae of live individuals between the pedicel and scape and immediately proceeded to the bending test experiments (Table S1). To perform a bending test, each antenna was placed in Dia-Stron brass crimps (Dia-Stron, UK) with its proximal end in the crimp; the distal end of the antenna was free to move. The brass crimp was placed on the corner of an elevated surface, with double-sided tape underneath to constrain the tube. The antenna was parallel to the ground, taking on the appearance of a cantilever beam (Figure 1a). A string with a weight at the end was hung next to the antenna as a reference for the direction of gravity. A portion of the brass tube of known diameter that was not crimped was visible for reference of the tube end position to ensure that all measurements followed the same boundary conditions (Figure 1b).

A set of 6–8 short copper wires of measured mass was prepared. A drop of adhesive (Gorilla Glue) was placed on the most distal end of the antenna. The copper wires were placed on the end of each antenna one by one while the process was recorded with a Point grey camera (FL3-

U3-13S2C-CS) and Grasshopper Camera (GS3-U3-23S6C-C) and FlyCapture® software. The relative weight of the copper wires was adjusted for each sample. For example, the larger *Manduca sexta* required an average weight of the copper wires of ~0.017 g, whereas the smaller *Xylophanes tersa* required a weight of ~0.006 g. Humidity in the testing room was 20–73% and temperature was 22℃–26℃ (Table 1 in Supplementary material). For *M. sexta*, 10 antennae were probed by bending them toward the dorsal and ventral sides. Three additional specimens were bent toward the dorsal side only and 3 more were bent toward the ventral side only. Five male antennae totaling 14 measurements and nine female antennae totaling 21 measurements were tested by bending the antennae perpendicular to the dorsoventral axis tested. *Ceratomia catalpae* had 4 trials toward the ventral side and 4 toward the dorsal side, whereas *M. quinquemaculata* and *X. tersa* had 3 trials each toward the ventral and dorsal directions. In all cases, antennae remained in the plane of bending. No spontaneous twisting of antennae was observed (Fig. 1c).

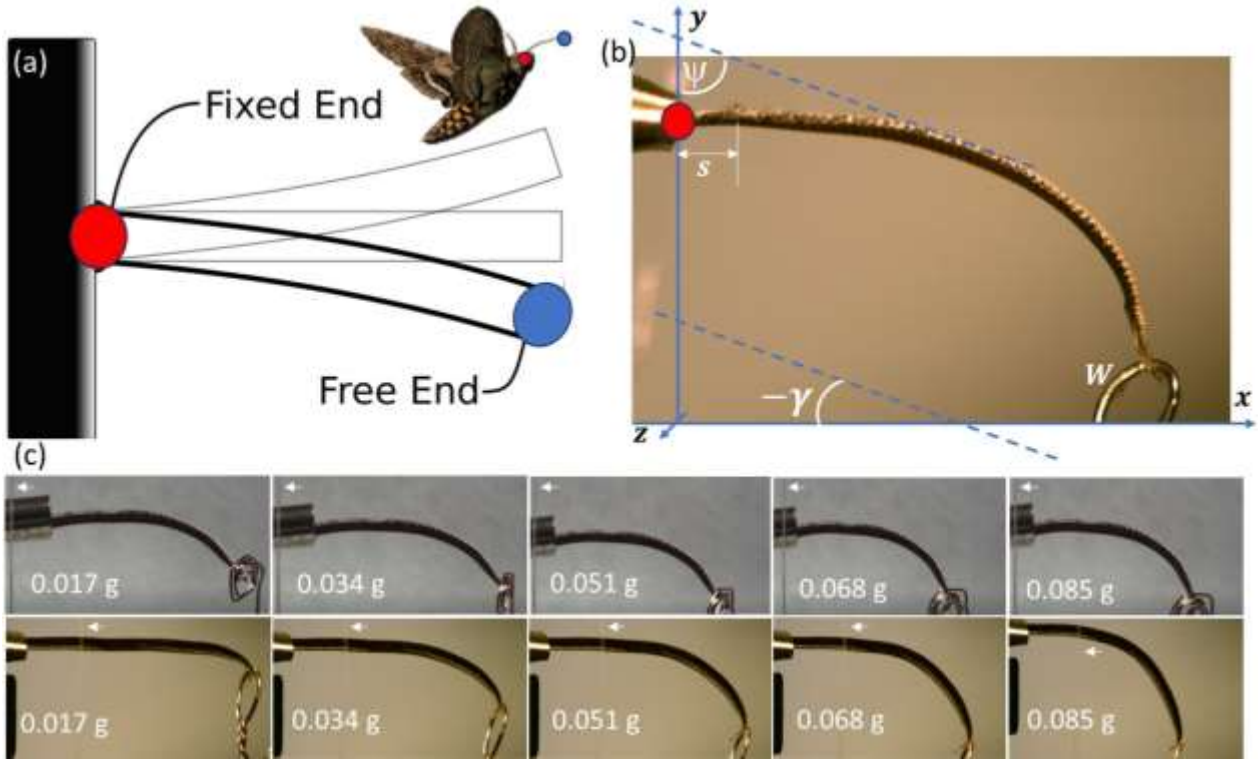

Figure 1. a) Cantilevered beam as an antenna model. In free flight, one end of the beam (blue dot) is free to move, and the other end (red dot) is fixed at the insect head. b) To study bending properties, the extracted antenna was fixed in a brass tube of known diameter (red dot) and a known weight W was attached to the other end of the antenna. In a Cartesian system of

coordinates, the antenna is bent in the (xy)-plane about the z-axis. The position along the antenna is measured by the arclength s, starting from the fixed end where $s = 0$. In the Euler elastica equation (1), an auxiliary angle ψ was introduced. This angle $\psi(s)$ is defined as the angle that the tangent line to the outermost dorsal side of the antenna at point s makes with the y-axis. The angle $\gamma(s)$ is defined as the angle that the tangent line to the outermost dorsal side of the antenna at point s makes with the x-axis. It is defined as positive when the antenna bends toward the dorsal side and negative when it bends toward the ventral side. c) Example images of antennal loading for male Manduca sexta towards the ventral side (upper row) and the dorsal side (lower row). The arrow points to a string indicating the direction of gravity. The wire diameter at the antenna end is 0.33 mm. One frame from the video of dorsal bending was shifted up to illustrate the full antennal bow in the last image in the lower row. The images confirm that the antenna remains in plane and does not twist during loading.

2.5. Contour extraction

Once the videos were obtained, screenshots of each antenna with its weight were obtained using Microsoft's snipping tool. Each of these images was individually analyzed in LabVIEW (NI 2020), with the contour being traced and exported into a .txt file. Due to a lack of available histology data, the second moment of inertia (SMI), $I^{\pm}$, for bending about the z-axis perpendicular to the antenna axis was taken as constant. The SMI was marked plus, I^{+}, when bending was toward the dorsal side of the antenna and minus, I^{-}, when it was toward the ventral side. Because no spontaneous twisting of antennae occurred (Fig. 1c), we used the beam equations for 2D bending. Therefore, the antenna bending equation was reduced to the Euler elastica equation written for each direction of bending as [29, 37]:

$$EI^{+}\,\frac{d}{ds}\left(\frac{d\psi}{ds}\right) - W\sin\psi = 0,\; EI^{-}\,\frac{d}{ds}\left(\frac{d\psi}{ds}\right) - W\sin\psi = 0\,. \tag{1}$$

where W is the applied weight, E is Young's modulus of the antenna obtained from the tensile test, s is the arclength measured from the point of antennal attachment, and ψ is the angle defined in Fig. 1. These equations were used in MATLAB to fit and estimate the flexural rigidities $f^{+} = EI^{+}$ and $f^{-} = EI^{-}$. For each guessed value $f^{\pm}$, we numerically solved the Euler elastica equations (1) by the shooting method[38] with two initial conditions $\psi(0) = \frac{\pi}{2};\; \frac{d\psi}{ds}(0) = u$. The parameter

u was changed until the condition at the antenna tip, $s = L$, $\frac{d\psi}{ds}(L) = 0$, where L is the length of the antenna, was satisfied. We then compared the theoretical solution with the experimental contour. If the theoretical contour did not fit the experimental one with the required accuracy, we searched for a new flexural rigidity $f^{\pm}$. These iterations continued until the accuracy criteria had been satisfied. The details can be found in the Supplementary material.

2.6. Second moment of inertia

To measure the second moment of inertia (SMI), the in-house MATLAB programs were developed to extract the contour and calculate the SMI. Using the MATLAB built-in edge detection algorithm in the Image Processing Toolbox, we developed the code to calculate the SMI. Once the contour was obtained, the code created a triangular mesh and provided the coordinates of the vertices. The coordinates were then processed to obtain the center of mass, area, and tensor of the second moments of inertia. The contours can be adjusted, and additional contours of interior elements could be added for exclusion in the SMI calculation.

2.7. Tensile testing

Tensile testing was done on a Micro Tensile Tester 2000 (Rheometric Scientific, US). The antennae were cut and placed on a C-shaped piece of paper with the middle of the antenna in the gap of the paper, and the ends were glued on the paper. The glue was applied so that it did not enter the antenna through the cut. The specimen was then placed in tensile clamps with thin pieces of cardboard to secure it. The portion of the C-shaped paper that bridged the two ends was cut so that the antenna was the only bridge between the clamps. While one end of the antenna remained fixed in a clamp, the other end was clamped to a moving stage that pulled the antenna, with tension, at a rate of 2 mm/min until the antenna broke. Tensile testing was recorded with Minimat software and saved to an Excel file for plotting. All antennae were tested at 22°C and 65% humidity to obtain the strain $\epsilon_{ss} = (L - L_0)/L_0$, where L is the length of antennal piece at the given load, L_0 is the initial length of the antennal bridge between the clamps.

Measurements of the flagellomere cross-sectional area A were obtained after an antenna was fractured in the tensile test; the thickness was evaluated at the crack, using a Huvitz light microscope (Model HR3-TRF-P). Five measurements were taken on *M. sexta* and were compared

with previous results to confirm that the measurements fell within the standard deviation[39]. Antennae of the other three hawkmoths were processed similarly. The stress was calculated as

$$\sigma_{\mathrm{ss}} = \frac{F}{A}, \tag{2}$$

where F is the force and A is the area of the cuticular shell.

To find the elastic modulus E, we grouped all data points for male antennae, and similarly but separately for female antennae, to find an average stress σ_{ss}^{break} and strain ε_{ss}^{break} at the point of antenna break. Then the stress and strains were normalized by the stress and strains at the point of the antenna break and the normalized stress-strain relations were generated. The normalized data were fitted with third-order polynomials. Visualization of antennal behavior during testing showed that at very small strains, the antennae straightened at almost zero stress. We found that the actual loading starts when the normalized strain in our dataset becomes greater than $\widehat{\epsilon_{\mathrm{ss}}} = 0.15$. Therefore, the obtained polynomials were used to calculate the elastic modules by taking derivative $\widehat{\mathrm{d}\sigma_{\mathrm{ss}}}/d\,\widehat{\epsilon_{\mathrm{ss}}}$ at $\widehat{\epsilon_{\mathrm{ss}}} = 0.15$ as

$$E = (\sigma_{ss}^{break}/\varepsilon_{ss}^{break}) \cdot (\widehat{\mathrm{d}\sigma_{\mathrm{ss}}}/d\,\widehat{\epsilon_{\mathrm{ss}}}) \text{ at } \widehat{\epsilon_{\mathrm{ss}}} = 0.15. \tag{3}$$

3. Results

3.1. Shapes of male and female antennae differ

The antennae of hawkmoths conform to the insectan ground plan, with a scape, pedicel, and flagellum [40] (Fig. 2). In addition, they are pectinate or comb-like; thus, they are not axisymmetric but instead are more strongly expressed toward the ventral side as pectinations, markedly so in males. The approximately 14,600 species of hawkmoths[41, 42] have a wide diversity of shapes and forms. Within the same species, male and female antennae differ in shape and length, with male antennae typically shorter and more comb-like than those of females [33-35, 43] (Fig. 2).

In all studied species, male antennae were widest at mid-length (Fig. 2f–m). The shape of female antennae, however, varied across species. Two species had clublike antennae that increased in width toward the tip (Fig. 2h, l); two other species had a shape similar to that of males (Fig. 2f, j). Thus, sexual dimorphism in overall antennal shape is expressed only in some species.

Male antennae are longer than those of females in our studied species, both with respect to overall body size and forewing length (Fig. 3 o, p). The shape and size differences between male and female antennae were not the same across species: males and females of the two *Manduca*

species had a much larger difference compared with *C. catalpae* and *X. tersa*, but all were sexually dimorphic.

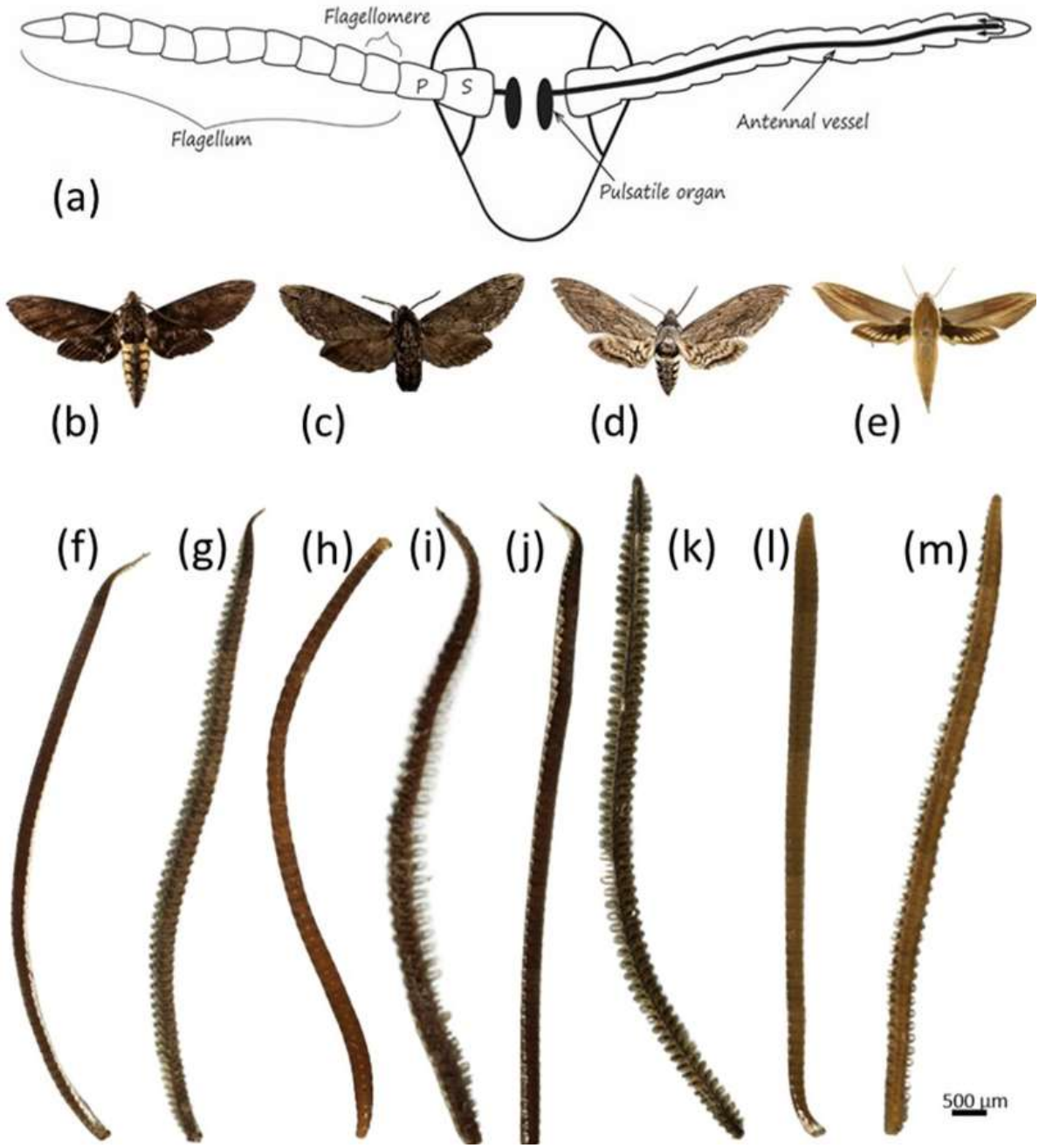

Figure 2. a) Schematic of the antennal ground plan of a generalized insect. Only the first two segments of the antenna, the scape (S) and pedicel (P), have muscles. The rest of the antenna, the

flagellum, is muscle free. The flagellum consists of a series of flagellomeres. Internal pulsatile organs pump blood (hemolymph) into the antenna through the antennal vessel, which terminates near the tip where hemolymph flows back to the head and moves through the lumen (hemocoel). b) Manduca sexta. c) Ceratomia catalpae. d) Manduca quinquemaculata. e) Xylophanes tersa. f) Female and g) male antennae of Manduca sexta. h) Female and i) male antennae of Ceratomia catalpae. j) Female and k) male antennae of Manduca quinquemaculata. l) Female and m) male antennae of Xylophanes tersa.

3.2. *The shapes of flagellomere cross sections of male and female antennae differ*

The shape of flagellomeres significantly affects the mechanical properties of antennae. The greatest difference between the sexes is in the antenna cross sections. The two sides of the antennae also differ [21, 39]; the dorsal side is covered with scales that can be easily removed. The flagellomeres of females are almost circular in cross section, whereas those of males have an expansion of the ventral cuticle in the shape of a keyhole (Figs. 3 g,j; 4). This expansion of multiple flagellomeres constitutes the pectination, which is well developed in males but less so in females. Hairs (fasciculate setae) on the ventral side of the flagellomeres of male hawkmoths are sense organs that serve various functions [33-35, 43]. In contrast, on the ventral side of female antennae the hair-like sense organs are much shorter.

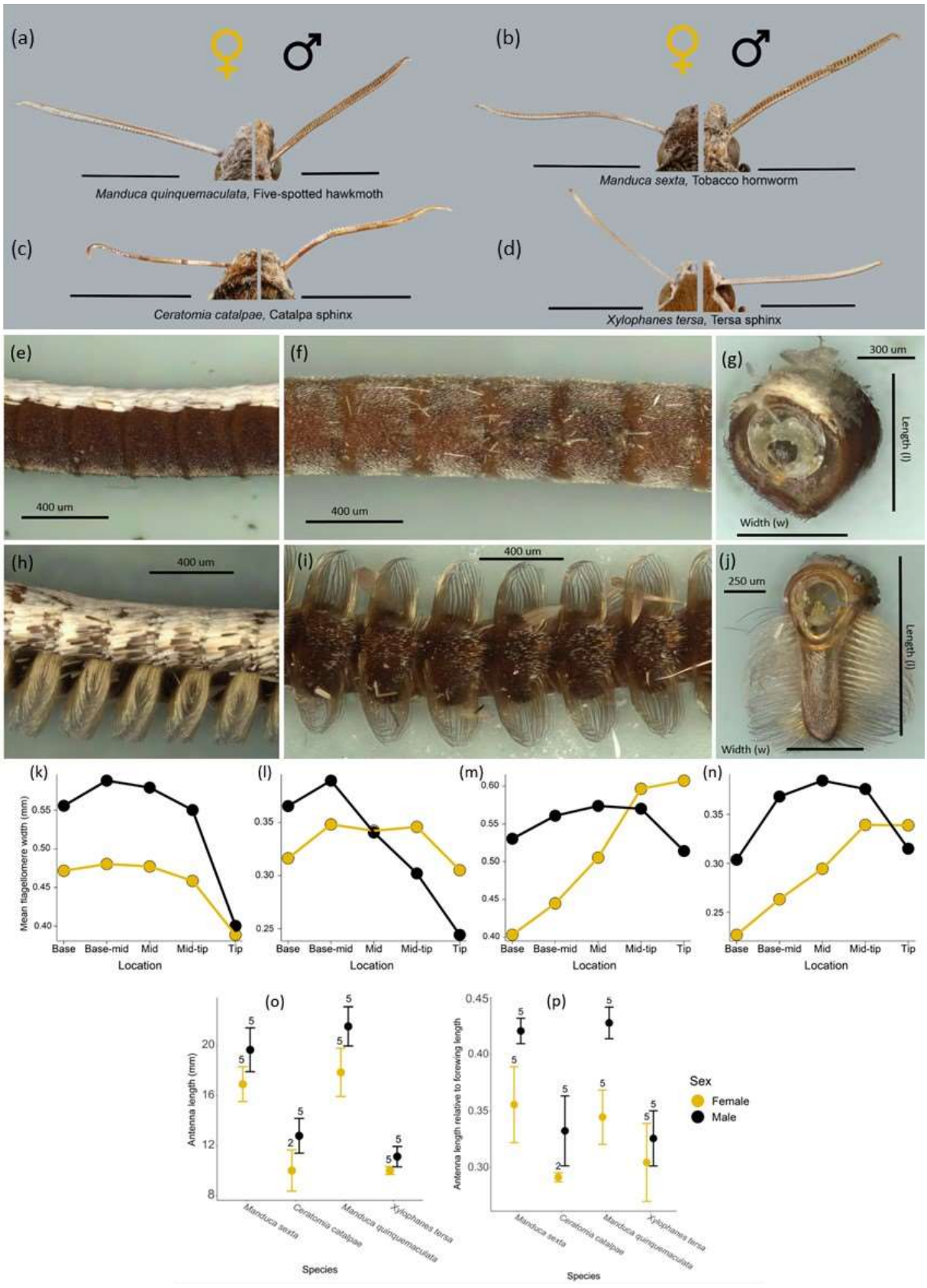
(a)
♀
♂
Manduca quinquemaculata, Five-spotted hawkmoth
(b)
♀
♂
Manduca sexta, Tobacco hornworm
(c)
Ceratomia catalpae, Catalpa sphinx
(d)
Xylophanes tersa, Tersa sphinx
(e)
400 um
(f)
400 um
(g)
300 um
Length (l)
Width (w)
(h)
400 um
(i)
400 um
(j)
250 um
Length (l)
Width (w)
(k)
Mean flagellomere width (mm)
0.55
0.50
0.45
0.40
Base
Base-mid
Mid
Mid-tip
Tip
Location
(l)
0.35
0.30
0.25
Base
Base-mid
Mid
Mid-tip
Tip
Location
(m)
0.60
0.55
0.50
0.45
0.40
Base
Base-mid
Mid
Mid-tip
Tip
Location
(n)
0.35
0.30
0.25
Base
Base-mid
Mid
Mid-tip
Tip
Location
(o)
Antenna length (mm)
20
16
12
8
5
5
5
2
5
5
5
5
Manduca sexta
Ceratomia catalpae
Manduca quinquemaculata
Xylophanes tersa
Species
(p)
Antenna length relative to forewing length
0.45
0.40
0.35
0.30
5
5
5
2
5
5
5
5
Manduca sexta
Ceratomia catalpae
Manduca quinquemaculata
Xylophanes tersa
Species
Sex
Female
Male

251

Figure 3. Quantitative metrics of sexual dimorphism in hawkmoth antennae. (a–d) Antennae of studied hawkmoths. (e–j) Antennal features of the antennae of Manduca sexta (e–g female, h–j male). (e, h) Lateral view. (f, i) Dorsal side view. (g, j) Flagellomere cross-sections and definitions of the width and length of pectinations used in the analysis. Measurements were taken for at least three flagellomeres per sex per species. k) Manduca quinquemaculata, l) Manduca sexta, m) Ceratomia catalpae, and n) Xylophanes tersa. Mean width (w) of flagellomeres in each section of the antennae. o) Average length (l) of antennae across species. p) Antenna length divided by forewing length across four species of hawkmoths. Dots represent the mean, bars the standard deviation, and numbers above bars the number of individuals measured.

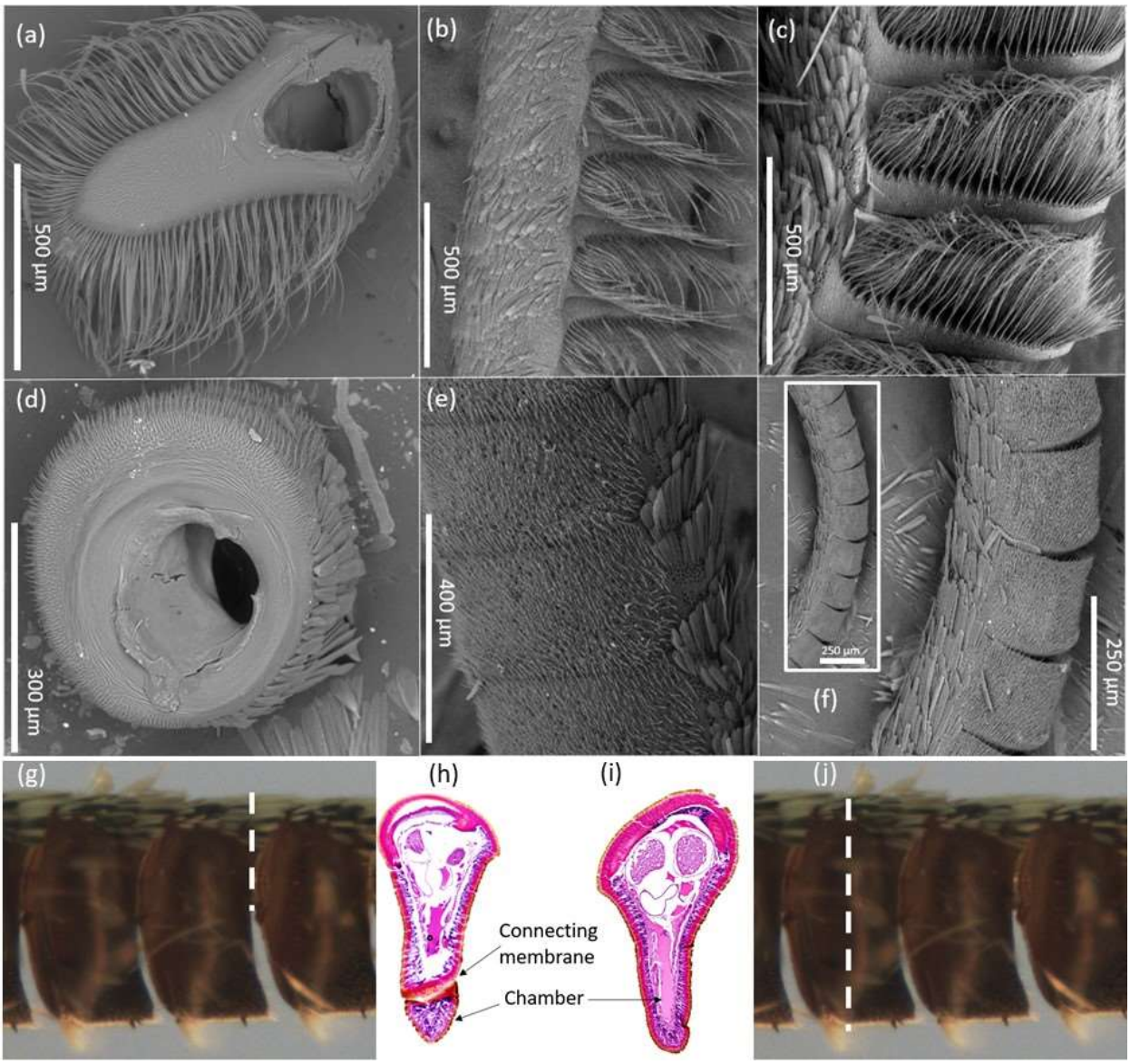

Figure 4. Sexual dimorphism in hawkmoth antennae. (a–f) Scanning electron micrographs. (a–c) Antenna of Manduca sexta male. (d –f) Antenna of M. sexta female. (a, d) Antennae were cut through the membrane

separating adjacent flagellomeres as shown in (g, h). The cuticular wall of the chamber remained intact; (a, d) the antennal lumen housed the antennal vessel, tracheae, and nerves, which collapsed on the cuticular wall after drying. (a) Long fasciculate setae are attached to the elongated chamber. (b, e) Lateral view of a straight section of antenna. (c, f) Lateral view of a bent section of antenna; inset in (f) shows the antennal arc. Flagellomeres spread apart on the outer curve when the antenna is bent from the ventral side toward the dorsal side. (h) Histological section of the male antenna of M. sexta through the connecting membrane, as shown in (g). The cuticle of the connecting membrane encloses a smaller area of the hemocoel. (i) Histological section of the male antenna of M. sexta through the entire flagellomere, as shown in (j). The flagellomere cuticle encloses a larger area of the hemocoel; tissue is visible in the chamber.

3.3. *Flexural rigidity*

The flexural rigidity $f^{-\pm}=EI^{\pm}$ in eq (1) characterizes the bending properties of the beam-like structures [31-33]. In this product f, the elastic modulus E reflects the materials properties of the cuticle, which may be anisotropic and dependent on the orientation of chitin crystals in the cuticle [34-37]. In tensile tests, this anisotropy cannot be revealed; therefore, we take E as a constant. The second moments of inertia $I^{\pm}$ reflect the structural organization of the antenna and can also be anisotropic [31].

As follows from the Euler elastica model, the antenna profile is controlled by a single dimensionless parameter $\tau = WL^2/f = WL^2/(EI)$. The greater the parameter τ, the more bent is the antenna (Fig. 5a). For a fixed weight W and antenna length L, the antennal flexibility is judged only by its flexural rigidity $f = EI$: the smaller the EI, the more flexible is the antenna (Fig. 5a).

The experimental profile of each antenna was fitted with the theoretical profile, using the Euler-elastica model (Fig. 5b). Afterwards, we averaged the f values obtained for each individual and, for *M. sexta*, we tested if the sex of the individual and the bending direction influenced f values. To do so, we used an ANOVA, with f as our dependent variable and sex (two levels, male and female), bending direction (two levels, dorsal and ventral), and their interaction as our independent variables. To understand where the significant differences resided, we used a Tukey HSD test as a *post-hoc* test.

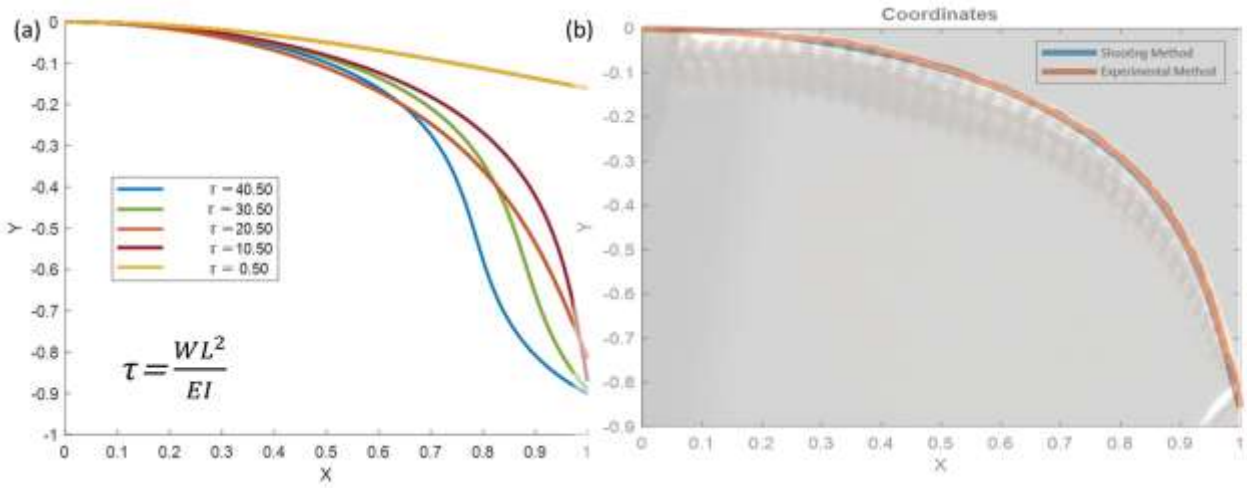

Figure 5 a) Theoretical profiles of antennae for different τ *. b) Illustration of the best fit of the antenna profile with the Euler elastica model. The antenna of Manduca sexta is shown on the background, and its dorsal side is contoured by the orange line. The blue curve is the Euler elastica fit. The flexural rigidity was* $f = 1.04\ nN \cdot m^2$.

Table 1. Flexural rigidity of Ceratomia catalpae, Xylophanes tersa, Manduca quinquemaculata, and Manduca sexta.

	Ceratomia catalpae	*Manduca quinquemaculata*	*Xylophanes tersa*	*Manduca sexta* (Male)	*Manduca sexta* (Female)
$f^+(nN \cdot m^2)$, antenna is bent toward the dorsal side	0.02 ± 0.014	1.58 ± 1.68	0.08 ± 0.03	1.05 ± 0.47	1.89 ± 0.34
$f^-(nN \cdot m^2)$, antenna is bent toward the ventral side	0.03 ± 0.02	2.07 ± 1.95	0.67 ± 0.53	1.45 ± 0.31	2.81 ± 0.86

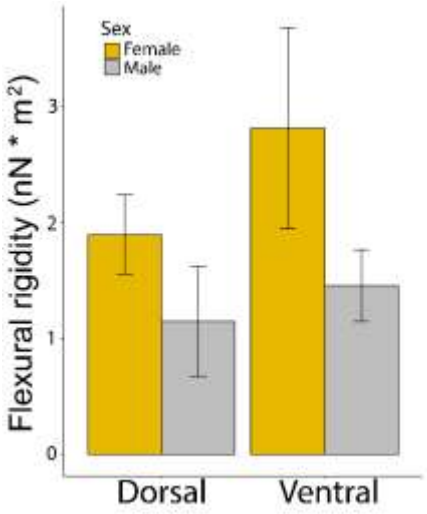

Figure 6. Average flexural rigidities of the antennae of Manduca sexta. The flexural rigidity depends on the direction of bending and sex of the hawkmoth.

We found significant sexual dimorphism in EI, showing that sex is an important factor in how antennae bend in hawkmoths ANOVA; $F_{3,10} = 4.709$, $p = 0.027$, $R^2 = 0.4612$; Fig. 6). The post-hoc test indicated that female antennae are stiffer than male antennae (Tukey HSD; $p = 0.008$). Specifically, female antennae were stiffer when bending to the ventral side (Tukey HSD; $p = 0.02$). All antennae resisted bending toward the ventral side where the pectinations are located. For example, when the antennae of males of *Manduca sexta* were bent toward the ventral side, the average flexural rigidity was $f = 1.45\ nN \cdot m^2$, whereas toward the dorsal side it was $f = 1.05\ nN \cdot m^2$. The flexural rigidities for bending toward the ventral side in *M. quinquemaculata*, *M. sexta*, and *X. tersa* were of the same order of magnitude $f \propto 10^{-9}\ N \cdot m^2$. Resistance for bending toward the dorsal side changed among species. Among the 4 species, *C. catalpae* had the most flexible antennae, with flexular rigidity about two orders of magnitude lower than that of the others, $f \propto 10^{-2}\ nN \cdot m^2$. Modeling the closing or opening of the V-angle of the antennal pair, we placed the antennae to face the camera either dorsally or ventrally. Bending the antennae of *M. sexta* perpendicular to the dorsoventral axis showed no statistically significant difference between males and females. Males had an average of $f = 1.47\ nN \cdot m^2$, whereas females had an average of $f = 1.60\ nN \cdot m^2$. ANOVA: for the males $p=0.929$, for the females, $p=0.439$, between all of the males and females, there was also no difference, $p = 0.569$. Thus, the flexural rigidity of antennae in the V-plane was lower, suggesting that antennae should be more reactive to wind gusting in the V-plane.

3.4. *Tensile properties of antennae of Manduca sexta*

To distinguish the contributions of materials properties of the antenna to flexural rigidity, we studied the tensile properties of the entire antenna. The test does not allow evaluation of the anisotropic properties of a single flagellomere but gives information on the mechanical reaction of the entire antenna to stretching. In a previous study[39], male and female antennae were analyzed

together, without attention to their structural differences. We detail the differences to evaluate how the tensile properties change between males and females.

Stress-strain relationships confirm that antennae of males and females do not indicate plasticity (Fig. 7). At small deformations, the antennae of males and females behave as a Hookean material. The average elastic modulus of male antennae is greater than that of females (Table 2).

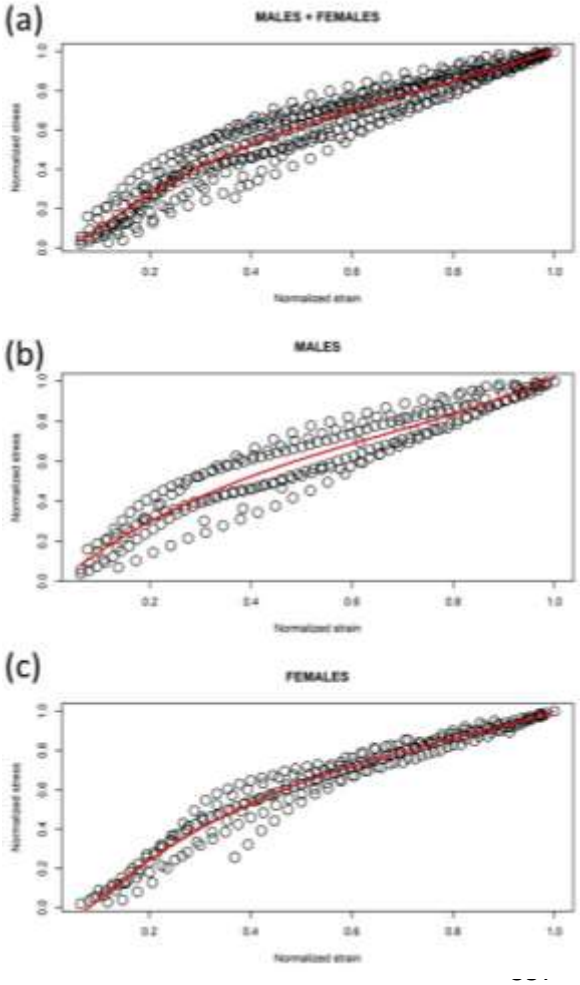

Figure 7. Characterization of the stress-strain relationship for antennae of Manduca sexta. Along the vertical axis is dimensionless stress, $\hat{\sigma}_{ss}$, defined as the ratio of stress normalized by the stress at the point of antenna break. Along the horizontal axis is the strain $\widehat{\epsilon_{ss}}$ normalized by the strain at the point of antenna break. The average trend lines are shown as solid curves. a) Males and females grouped together; the trendline is represented as $\hat{\sigma}_{ss} = 0.3260 * \widehat{\epsilon_{ss}}^3 - 0.8098 * \widehat{\epsilon_{ss}}^2 + 5.6656 * \widehat{\epsilon_{ss}} + 0.6313$; *b) Males, the trendline is represented as* $\hat{\sigma}_{ss} = 0.2522 * \widehat{\epsilon_{ss}}^3 - 0.3811 * \widehat{\epsilon_{ss}}^2 + 3.9195 * \widehat{\epsilon_{ss}} + 0.6234$; *c) Females; the trendline is represented as* $\hat{\sigma}_{ss} = 0.2455 * \widehat{\epsilon_{ss}}^3 - 0.7884 * \widehat{\epsilon_{ss}}^2 + 4.0934 * \widehat{\epsilon_{ss}} + 0.6393$.

Table 2. Average Young's modulus for antennae of *Manduca sexta*.

	Young's modulus measured with hemolymph inside (GPa)
Average, E (Male)	0.10 ± 0.03
Range (Male)	$0.05 < E < 0.17$
Average, E (Female)	0.08 ± 0.02
Range (Female)	$0.05 < E < 0.12$

Table 3. Average stress and strain at break for antennae of *Manduca sexta*.

	Male	Female
Average stress (MPa)	8.33 ± 4.06	6.61 ± 2.72
Average strain (%)	14.61 ± 4.84	13.46 ± 3.98

3.5. *Connecting flexural rigidity with histology*

The structural contribution to flexural rigidity comes from the second moment of inertia of the flagellomeres and connecting membranes. The cuticular walls of the flagellomeres and connecting membranes taking up the load are distinctly shaped (Fig. 4g–j). When the antenna is bent toward the ventral side, the pectinations come together and press against one another. The antenna in this case reacts to bending as a continuous beam without pectinations, but its shape follows that of the individual flagellomeres. In contrast, when the antenna is bent toward the dorsal side, the pectinations spread apart and the main load is taken up by the connecting membranes (Fig. 8).

We validated the experimentally measured flexural rigidities by calculating flexural rigidity, using the experimental Young's modulus and analyzing the second moments of inertia for pectinations and connecting membranes from histology. The main problem with calculation of the second moment of inertia is the difficulties in obtaining images of the antennal cross-section that contain the connecting membrane and pectination. Also, the flagellomere cross-section changes along antennae; therefore, with a few images per antenna, we can only provide an order of magnitude estimate of the average second moment of inertia. The histology of antennae requires special attention, particularly achieving a cross-section at the connecting membrane between flagellomeres (Fig. 4g) and will be discussed elsewhere.

The explanations of the numeric algorithm for calculation of the second moments of inertia are given in the Supplementary material. While the match between theoretical and experimental flexural rigidities is not ideal, the trend is confirmed (Table 4).

Figure 8. Schematic of antennal reaction to wind load. The direction of the wind is shown by the arrows, and the pectinate antennae of hawkmoths is modeled by a comb. a) When the wind bends antennae from the dorsal to the ventral side, the flagellomeres (like the comb bristles) come together to resist the load. The stress is distributed over the entire flagellomere cuticle. Thus, the triangulation area for calculation of the moment of inertia embraces the entire cuticular wall of the flagellomere highlighted in pink in the histological section and reflected in the schematic on the far right. b) When the wind bends antennae from the ventral to the dorsal side, the flagellomeres spread apart and the load is distributed mostly on the connecting membranes. Thus, the triangulation area for calculation of the moment of inertia embraces only the cuticular wall of the connecting membrane highlighted in pink in the histological section and reflected in the schematic on the far right.

Table 4. Comparison of calculated theoretical and experimental flexural rigidities. The average second moment of inertia, $I^{\pm}$, is calculated from histology images. The standard deviations (STDEV) from the averaged $I^{\pm}$ are shown in a separate column. The average Young's modulus E taken from Table 2 were used to calculate theoretical flexural rigidities $f^{\pm} = EI^{\pm}$ for bending antennae about the z axis toward the dorsal (plus) and ventral (minus) directions. The experimental values are shown for comparison.

Number of images	Sex and direction of bending	Average $I^{\pm}$, from histology (mm^4)	STDEV (mm^4)	Average experimental E (GPa)	Average theoretical $f^{\pm}$ ($nN \cdot m^2$)	Average experimental $f^{\pm}$ ($nN \cdot m^2$)
5	Male, bending toward ventral side	0.0139	0.002	0.10	1.39	1.45
1	Male, bending toward dorsal side	0.0082			0.82	1.05
2	Female, bending toward ventral side	0.034		0.08	2.70	2.81
1	Female, bending toward dorsal side	0.016			1.28	1.89

4. Discussion

The neuromechanical response of hawkmoth antennae to environmental perturbations suggests that the flagellum reacts to the wind as a rigid rod pivoting at the antennal base where the first segment (i.e., scape) articulates with the head capsule, and the torque exerted by the wind on the flagellum is detected by sensing organs at the flagellum–pedicel–scape joints [3, 14, 15, 17, 22, 23, 40, 44, 45]. Hawkmoth antennae have been suggested to work as gyroscopes without which stable flight and hovering would not be possible [17]. These conclusions were based on a 2D analysis of the V-angle dynamics of antennae. *Manduca sexta* with amputated antennae can take off and fly [46], raising questions about the gyroscopic nature of antennae and the critical role of antennae in flight control. The rigid-rod model, while attractive for its simplicity, does not fully appreciate the diversity of antennal morphology and associated movement dynamics. The lack of mechanical analysis of the 3D movement of antennae prevents interpretation of our results in the context of the role of antennae in flight stabilization.

We suggest that hawkmoths take advantage of their pectinate antennae to sense the strength and direction of the wind and wind-borne olfactory cues (e.g., pheromones). As we have shown for all tested species, flexural rigidity is greater when the antenna is bent toward its ventral side. Thus, the antennae could easily be flexed toward the dorsal side, exposing sensory organs there to wind gusts. In forward flight when upwind disturbance from flapping wings decreases, the wind direction can be probed by the wind-facing sensilla[16], allowing male hawkmoths to track odor plumes. Our results allow us to evaluate this idea by estimating antennal deflections, using a model of a cantilevered beam[47], after first determining when the antenna can be modeled as a rigid rod.

The antenna as a rigid rod. For the rigid-rod model, we assume that the antennal tip does not deflect appreciably with respect to the pedicel–scape pair at the base. The tip deflection of the initially straight antenna on a load w, distributed uniformly over its length L, is [47]:

$$\delta = wL^4/(8f). \quad (4)$$

We first consider the antenna deflection by its own weight, assuming the antennal cross section is constant; for this case, $w = g(\rho_{wall}A_{wall} + \rho_{hemolymph}A_{hemocoel})$, where g is the acceleration due to gravity, ρ is the density, A is the cross section, and the indices specify the objects. For an order of magnitude estimate, we set $\rho_{wall} \approx \rho_{hemolymph} \approx \rho_{water} = 10^3\ kg/m^3$, then $A_{wall} + A_{hemocoel} = A$, the area of the antennal cross section including the cuticular wall and hemocoel. For an upper order of magnitude estimate, one can use the width W and height H of the largest flagellomeres to get $A < W \cdot H$. For example, the tip deflection of the antenna of males of *M. sexta*, with $A \approx 2.4 \cdot 10^{-8}\ m^2$, is estimated as $\delta < g \cdot \rho_{water} \cdot A \cdot L^4/(8f) \approx 1.6 \cdot 10^{-3}\ m$. Thus, under its own weight, the antennal tip deflects less than ~10% of its length. In this scenario, the rigid-rod model can be used for the description of antennae in still air.

Estimation of antennal deflection by aerodynamic forces. To apply eq. (4) to the estimation of antennal deflection, we need to specify the regime of the air flow around antennae, whether it is controlled by inertial or viscous forces. For an upper estimate of the dynamic load, we consider the most vigorous forward flight where antennae are subject to a strong wind with velocity U that could be as high as $U \sim 1 - 4\ m/s$ for *M. sexta* [16, 46]. In the inertia-controlled regime of air flow, air viscosity η_{air} plays no role; in contrast, for viscosity-controlled air flow, the air density ρ_{air} plays no role[48]. Accordingly, the drag on the antenna in the inertia-controlled regime is proportional to the velocity squared, whereas in the viscosity-controlled regime it is linearly proportional to velocity[24, 48].

To evaluate the flow regime, we calculated the Reynolds number for flow associated with rotation of antennae about the z-axis. Thus, one needs to classify the regime of quasi-two-dimensional flow past each flagellomere. If U is the magnitude of the air velocity in the direction of forward flight, and the antenna is tilted by angle γ with respect to the flight direction, the

magnitude of velocity perpendicular to the antenna considered as a rigid rod is $U_\perp = U \cdot \sin\gamma$. Thus, the smaller the tilt angle γ, the smaller the velocity $U_\perp \approx U\gamma$. The Reynolds number is defined as $Re = \rho_{air} \cdot U \cdot \tan\gamma \cdot H/\eta_{air}$, where H is the largest flagellomere dorsoventral length as defined in Fig. 3g, j. For males of *M. sexta*, the largest flagellomere length including fasciculate setae is H~ 1 mm; using $\eta_{air}/\rho_{air} \approx 1.5 \cdot 10^{-5} m^2/s$ for the air at 15℃, and taking $U = 4\, m/s$, we estimate the Reynolds number as $Re = 0.66 \cdot 10^5 \cdot 4 \cdot 10^{-3} \cdot \sin\gamma \cdot\!= 2.6 \cdot 10^2 \cdot \sin\gamma$. Thus, for the small tilt angles $\gamma < 0.01$ (or $\gamma < 1°$), the air flow is mostly controlled by air viscosity. For larger angles, it is controlled by air inertia.

We were not able to find data on dorsoventral deflection of antennae in flying hawkmoths. The focus of research so far has been on analysis of sidewise deflection of antennae changing the V-angle of the antenna pair[15, 17]. During forward flight, the sidewise drag on antennae is significant, as the antennae are appreciably angled with respect to the flight direction. The Gewecke-Heinzel theory[28], allowing evaluation of the torque on the pivot of a rigid-rod, has been used so far as an input for a neuromechanic model of antenna flight control[15].

In contrast to the V-positioning, the dorsoventral posture of antennae could be in the plane of the upwind flow. This posture may not be stable, as small fluctuations of the antenna profile could be amplified by the aerodynamic force. At small deflections from the straight antennal configuration, the velocity component normal to the antenna direction is proportional to $\sin\gamma$, or to $\sin\gamma \sim \gamma$. While the antennal deflection could be small, eq.(4) cannot be directly applied to find it because the drag w depends on the local deflection $\gamma(s)$ that has to be determined.

For a steady forward flight, we need to use the force balance like that in eq.(1), but modify it to include the aerodynamic force [49] as shown in the Appendix. The results of these calculations showed that the straight antenna is not stable and is subject to bending when the upwind velocity becomes greater than the critical value

$$U^{\pm} = \sqrt{2EI^{\pm}} \Big/ \sqrt{\frac{dC}{d\gamma} \cdot \rho_{air} \cdot AL^2}, \qquad (5)$$

where $C(\gamma)$ is a drag coefficient of the antenna, limiting the lift force as a function of the angle of attack γ, A is the cross-sectional area, and L is the length of the antenna. For an order of magnitude estimate of the critical velocity, when this instability would first show up, we assume that $\frac{dC}{d\gamma} \sim 1$,

$A \sim 10^{-7}\ m^2$ and $L \sim 0.1\ m$. This gives $U^{\pm} \sim 1 m/s$. Thus, at the velocities typically observed in forward flight of hawkmoths[16, 46], one expects the antennae to deflect from their straight configuration. For the deflection towards the dorsal side, the velocity barrier is lower than that for the deflection towards its ventral side, $\frac{U^+}{U^-} = \sqrt{I^+}/\sqrt{I^-}$. For *M. sexta* males, this ratio is about 0.9 and for females it is 0.8.

Biological implications of antennal properties. Hawkmoths can sense and control the antennal V-angle [15, 17]; our estimates of the difference in the conditions for dorsoventral deflection in *M. sexta*, while small, seem to be detectable by the same sensing organs at the pedicel–scape pair. Therefore, flexural anisotropy of antennae could be useful for evaluation of the upwind strength and fluctuations of the wind direction.

Nearly the same stiffness of male and female antennae points to the importance of antennal morphology in setting up the sensitivity barriers for detecting upwind velocities. Flagellomeres in female antennae are separated by narrow ~ 20 μm gaps (Fig. 4e), whereas these gaps in male antennae are much larger, ~ 50 μm (Fig. 4b). These antennae were imaged in their resting, straight configurations. Thus, when bent towards the ventral side, the adjacent flagellomeres of females come in contact almost immediately, making the antennal bow shallow, and offering a high flexural resistance. In contrast, the adjacent flagellomeres with well-developed pectinations of males have room to move freely until they contact one another. As a result, the male antennae appear more flexible.

More flexible antennae could more easily differentiate small changes in the wind strength and its direction. Electrical engineers named the “whip antenna”[50], probably drawing from insect antennae that can move as a whip when perturbed. Like a flapping banner that reacts to a minute change in the wind, the male antenna could respond to small changes in wind gusts when its speed reaches the critical speed for instability development. To distinguish the same wind features, the less flexible antennae of females would require greater differences in equation (5) for the dorsal versus ventral deflection.

Despite simplicity of the idealized model, equation (5) provides an important relation between the antennal materials properties and morphological characteristics. The model ignores antennal deflection in the plane of the air stream changing the V-angle. Moreover, hawkmoth antennae are not axisymmetric, and are prone to twist. The asymmetry of the antennal cross section implies that

518 the aerodynamic loading cannot be reduced only to external forces: one cannot ignore the
519 aerodynamic torque acting to twist the antennae[49]. Future 3D visualization of antennal
520 movement during flight is necessary to examine whether antennae experience twisting, and, if so,
521 how the insect deals with it.

522 Dimorphism in insects manifests in various characters including size, ornamentation,
523 coloration, and weaponry[40]. The structural differences of antennae between male and female
524 hawkmoths have long been known[33-35, 51]. The distinct flexural rigidities bring together the
525 morphological features and biomechanics associated with feeding and mating. Males and females
526 of most hawkmoth species feed on floral nectar and share many of the same nectar sources, but
527 their foraging behavior differs, with males typically flying longer distances than females [52]. The
528 forewing shape of male hawkmoths suggests adaptation for faster flight, such as during mate
529 searching, whereas wing shape of females suggests adaptation for slower flight, perhaps during
530 host-plant searching for oviposition sites[53]. This dimorphism in behavior and wing structure
531 would be expected to have sex-differential consequences for antennae, given the different wind
532 speeds encountered and the executed maneuvers. The sensory system of male antennae should be
533 more robust, serving not only for searching for flowers but also for mates. Having more flexible
534 antennae allows male hawkmoths to swipe a larger air volume to detect a pheromone plume during
535 flight[51, 54]. Non-feeding hawkmoths, *Ceratomia catalpa* in our example, have the most flexible
536 antennae. Their antennae are not designed to withstand severe wind loads and are needed to screen
537 the air only for pheromones and perhaps host-plant cues for oviposition.

538 Insect antennae vary dramatically in structure but can generally be categorized as one of 10
539 forms, pectinate among them[55]. Although the functional value of some antennal forms, such as
540 plumose antennae for enhanced capture of air-borne chemicals, is well documented, that of other
541 forms lacks experimental evaluation. Pectinate antennae have evolved multiple times in
542 taxonomically diverse taxa, such as beetles and moths. We recognize that this antennal form might
543 serve different functions in insects, such as in flying versus nonflying insects, but we also expect
544 that the effects of bending toward the pectinations would be similar.

545 We emphasize that antennae and flight are strongly associated; wind currents produced by the
546 wings have consequences for the antennae and their ability to provide optimal sensory function,
547 including feedback to control flight. Rapid shifts not only in the direction of flight, but also from
548 forward flight to swing-hovering flight in hawkmoths cause antennal deformations. The pectinate,

549 yet robust, antennae of these moths represent an evolutionary compromise between the conflicting
550 demands of rapid flight (up to 5.3 m/sec [56]) and sensing of food, mates, and host plants. Thus,
551 we suggest that wing shape and antennal form represent an example of correlated evolution, with
552 hawkmoth antennae the result of an evolutionary compromise between selection and
553 counterselection. Speed and maneuverability have evolved in the context of maintaining a highly
554 sensitive yet stable sensory system. Increased antennal surface area translates to more sensilla,
555 such as fasciculate setae in male hawkmoths, but carries the risk of increased drag and wild
556 oscillations of the antennae. When these pressures are relaxed, antennal plumosity for greater
557 sensing capability reaches the zenith of development in the giant silk moths (family Saturniidae).
558 Giant silk moths are the sister clade of hawkmoths but have large wing to body ratios that translate
559 to an entirely different flight strategy based on slow, high-amplitude wing strokes [57]. These
560 flight characteristics would create less antennal drag and perturbation during flight, minimizing
561 the need for air-flow control during typical flight conditions. Hawkmoths routinely deal with
562 changes in air flow created by wing flapping, wind gusts, and the wake of flowers produced during
563 hovering[58] Additional environmental factors, such as rain, compound the risk of antennal
564 perturbation. We have, for example, observed hawkmoths flying and foraging during light to heavy
565 rains. Accordingly, robust antennae with pectinations that offer anisotropy to damp deformations
566 would be expected to broaden the environmental conditions under which hawkmoths can fly.

567 An examination of insects in diverse groups would be profitable in revealing the extent of non-
568 axisymmetric antennae, anisotropy, and the adaptive significance of antennal form in the context
569 of behavior. Longhorn beetles (family Cerambycidae), for example, offer a model taxon for
570 exploring the biomechanics of antennae. These beetles exhibit a range of antennal forms in which
571 anisotropy would be expected, particularly in those with exaggerated pectination such as some
572 species of the genus *Prionus*. We predict that antennal anisotropy, manifesting context-dependent
573 advantages, will be widespread among insects.

574 From engineering standpoint, our work offers promising new applications of shaped fibers[59] as
575 mechanical sensors.

576 **Conclusion**

Our comparative analysis of mechanical properties of hawkmoth antennae revealed a new feature: resistance to bending toward the dorsal side is less than that toward the ventral side. The pectinate antennae of hawkmoths behave as a comb in which the bristles resist bending when they come together. The bending properties of antennae in males and females differ, broadening the range of sexual dimorphism in Lepidoptera. Although the lack of 3D visualization of antennal behavior during flight prevents predictive modelling of the neuromechanics, we established a reference for future studies that would bring together the mechanical response of antennae to aerodynamic loading and the neural response to controlling flight.

5. Acknowledgements

This work was partially supported by the NSF grant IOS 2014664, by the Clemson University Creative Inquiry project to KK, and by the SC BioCRAFT facilities supported by the National Institute of General Medical Sciences (NIGMS) of the National Institutes of Health under award number P30GM131959 through the voucher program to KK, and by an appointment to the Department of Defense (DOD) Research Participation Program administered by the Oak Ridge Institute for Science and Education (ORISE) through an interagency agreement between the U.S. Department of Energy (DOE) and the DOD. ORISE is managed by ORAU under DOE contract number DE-SC0014664. All opinions expressed in this paper are those of the authors and do not necessarily reflect the policies and views of DOD, DOE, or ORAU/ORISE. We thank M. L. Ferro, Collection Manager of the Clemson University Arthropod Collection, for allowing us to use hawkmoths in the collection. We thank L. Marsh for helping with the antenna bending experiments. The work of P.H.A. was partially supported by NIFA/USDA under project number SC-1700596 and is Technical Contribution No. 7289 of the Clemson University Experiment Station.

Appendix

Consider an idealized case of a velocity field **U** parallel to the antenna axis, the x-axis in Fig.1. In an unperturbed state, the antenna is straight. As the insect moves its head, the antenna is allowed to deflect from the original configuration and we question at which velocity antenna flapping is expected. In a steady state flight, the antenna profile is described by the following equation[49]

606 $$f^{\pm}\frac{d}{ds}\left(\frac{d\gamma^{\pm}}{ds}\right)+\alpha^2\gamma^{\pm}=0\,. \qquad \alpha^2=(\frac{dC}{d\gamma})\rho_{air}U^2\cdot A/2, \tag{A1}$$

607 where in eq.(1) we expressed ψ as $\psi(s)=\frac{\pi}{2}\pm\gamma^{\pm}(s)$ and replaced the weight on the antenna
608 end with the aerodynamic force; C is the lift coefficient which is a function of the angle of attack
609 γ defined in Fig. 1, A is the cross-sectional area of a flagellomere. The solution of eq.(A1) is

610 $$\gamma^{\pm}=A^{\pm}\cos(\beta^{\pm}s)+B^{\pm}\sin(\beta^{\pm}s),\text{ where }\beta^{\pm}=\alpha/\sqrt{EI^{\pm}}\ . \tag{A2}$$

611 Assuming that the flagellum is fixed at the angle $\psi(0)=\frac{\pi}{2}$ and no bending is acting on the
612 antenna free end, we set up the following boundary conditions for eq.(A2)

613 $$\gamma^{\pm}(0)=0, \qquad \frac{d\gamma^{\pm}}{ds}(L)=0. \tag{A3}$$

614 Substituting eq.(A2) in eqs.(A3), we find
615
616 $$A^{\pm}=0,\cos(\beta^{\pm}L)=0,=>\ \beta^{\pm}L=\frac{\pi}{2}+\pi n, n=0,1,2,3\ldots. \tag{A4}$$

617 Thus, the first nontrivial solution will appear at n=0, corresponding to the velocity

618 $$U^{\pm}=\sqrt{EI^{\pm}}/\sqrt{\frac{dC}{d\gamma}\cdot\rho_{air}\cdot A/2}. \tag{A5}$$

619 The small deflections $u^{\pm}(x)$ are determined from equation $\gamma^{\pm}(s)\approx\gamma^{\pm}(x)\approx du^{\pm}/dx$ and
620 condition $u^{\pm}(0)=0$ as

621 $$u^{\pm}(x)=\pm(B^{\pm}/\beta^{\pm})(1-\cos(\beta^{\pm}x)), \tag{A6}$$

622 where $B^{\pm}$ needs to be found from the second order approximation. Equation (A6) shows that the
623 perturbed antenna is prone to form a profile corresponding to a quarter period of a cosine function.

624 **References**

625

1. Misof, B., Liu, S.L., Meusemann, K., Peters, R.S., Donath, A., Mayer, C., Frandsen, P.B., Ware, J., Flouri, T., Beutel, R.G., et al. (2014). Phylogenomics resolves the timing and pattern of insect evolution. Science *346*, 763-767.
2. Schneider, D. (1964). Insect antennae. Annual Review of Entomology *9*, 103-&.
3. Krishnan, A., and Sane, S.P. (2015). Antennal mechanosensors and their evolutionary antecedents. In Advances in Insect Physiology, Vol 49, Volume 49, R. Jurenka, ed. (London: Academic Press Ltd-Elsevier Science Ltd), pp. 59-99.
4. Boeckh, J., Kaissling, K.E., and Schneider, D. (1965). Insect olfactory receptors. Cold Spring Harbor Symp. Quant. Biol. *30*, 263-+.
5. Kaissling, K.E. (1998). Flux detectors versus concentration detectors: Two types of chemoreceptors. Chem. Senses *23*, 99-111.
6. Kanaujia, S., and Kaissling, K.E. (1985). Interactions of pheromone with moth antennae - adsorption, desorption and transport. Journal of Insect Physiology *31*, 71-81.
7. Koehl, M.A.R. (1996). Small-scale fluid dynamics of olfactory antennae. Marine and Freshwater Behaviour and Physiology *27*, 127-141.
8. Daly, K.C., Kalwar, F., Hatfield, M., Staudacher, E., and Bradley, S.P. (2013). Odor detection in *Manduca sexta* Is optimized when odor stimuli are pulsed at a frequency matching the wing beat during flight. Plos One *8*.
9. Kadakia, N., Demir, M., Michaelis, B.T., DeAngelis, B.D., Reidenbach, M.A., Clark, D.A., and Emonet, T. (2022). Odour motion sensing enhances navigation of complex plumes. Nature *611*, 754-+.
10. Mafraneto, A., and Carde, R.T. (1994). Fine-scale structure of pheromone plumes modulates upwind orientation of flying moths. Nature *369*, 142-144.
11. Staudacher, E.M., Gebhardt, M., and Durr, V. (2005). Antennal movements and mechanoreception: Neurobiology of active tactile sensors. In Advances in Insect Physiology, Vol 32, Volume 32, S.J. Simpson, ed., pp. 49-205.
12. Gewecke, M. (1970). Antennae - another wind-sensetive receptor in Locusts Nature *225*, 1263-&.
13. Gewecke, M. (1974). The antennae of insects as air-current sense organs and their relationship to the control of flight. In Experimental analysis of insect behaviour, L.B. Browne, ed. (Springer), pp. 100-113.
14. Krishnan, A., Prabhakar, S., Sudarsan, S., and Sane, S.P. (2012). The neural mechanisms of antennal positioning in flying moths. Journal of Experimental Biology *215*, 3096-3105.
15. Natesan, D., Saxena, N., Ekeberg, O., and Sane, S.P. (2019). Tuneable reflexes control antennal positioning in flying hawkmoths. Nature Communications *10*.
16. Sane, S.P., and Jacobson, N.P. (2006). Induced airflow in flying insects - II. Measurement of induced flow. Journal of Experimental Biology *209*, 43-56.
17. Sane, S.P., Dieudonne, A., Willis, M.A., and Daniel, T.L. (2007). Antennal mechanosensors mediate flight control in moths. Science *315*, 863-866.
18. Steinbrecht, R.A. (1997). Pore structures in insect olfactory sensilla: A review of data and concepts. International Journal of Insect Morphology & Embryology *26*, 229-245.
19. Nishino, H., Iwasaki, M., Paoli, M., Kamimura, I., Yoritsune, A., and Mizunami, M. (2018). Spatial Receptive Fields for Odor Localization. Current Biology *28*, 600-+.
20. Wicher, D. (2015). Olfactory Signaling in Insects. In Molecular Basis of Olfaction, Volume 130, R. Glatz, ed. (San Diego: Elsevier Academic Press Inc), pp. 37-54.
21. Stockl, A.L., and Kelber, A. (2019). Fuelling on the wing: sensory ecology of hawkmoth foraging. Journal of Comparative Physiology a-Neuroethology Sensory Neural and Behavioral Physiology *205*, 399-413.

22. Suver, M.P., Medina, A.M., and Nagel, K.I. (2023). Active antennal movements in *Drosophila* can tune wind encoding. Current Biology *33*, 780-+.
23. Claverie, N., Buvat, P., and Casas, J. (2023). Active sensing in bees through antennal movements Is independent of odor molecule. Integrative and Comparative Biology.
24. Humphrey, J.A.C., and Barth, F.G. (2007). Medium flow-sensing hairs: Biomechanics and models. In Advances in Insect Physiology: Insect Mechanics and Control, Volume 34, J. Casas, ed. (San Diego: Elsevier Academic Press Inc), pp. 1-80.
25. Taylor, G.K., and Krapp, H.G. (2007). Sensory systems and flight stability: What do insects measure and why? In Advances in Insect Physiology: Insect Mechanics and Control, Volume 34, J. Casas, ed., pp. 231-316.
26. Johnson, B. (1956). Function of the antennae of aphids during flight. Australian Journal of Science *18*, 199-200.
27. Yagodin, S.V., and Kovbasa, S.I. (1984). The flight maintenance in the cockroach *Periplaneta americana L*. Journal of Comparative Physiology *155*, 697-712.
28. Gewecke, M., and Heinzel, H.G. (1980). Aerodynamic and mechanical properties of the antennae as air-current sense organs in *Locusta Migratoria*. 1. Static characteristics. Journal of Comparative Physiology *139*, 357-366.
29. Mongeau, J.M., Demir, A., Dallmann, C.J., Jayaram, K., Cowan, N.J., and Full, R.J. (2014). Mechanical processing via passive dynamic properties of the cockroach antenna can facilitate control during rapid running. Journal of Experimental Biology *217*, 3333-3345.
30. Mongeau, J.M., Sponberg, S.N., Miller, J.P., and Full, R.J. (2015). Sensory processing within cockroach antenna enables rapid implementation of feedback control for high-speed running maneuvers. Journal of Experimental Biology *218*, 2344-2354.
31. Wainwright, S.A., Biggs, W.D., Currey, J.D., and Gosline, J.M. (1982). Mechanical Design in Organisms (Princeton University Press).
32. Keil, T.A. (2012). Sensory cilia in arthropods. Arthropod Structure & Development *41*, 515-534.
33. Sanes, J.R., and Hildebrand, J.G. (1976). Structure and development of antennae in a moth, *Manduca sexta*. Developmental Biology *51*, 282-299.
34. Shields, V.D.C., and Hildebrand, J.G. (1999). Fine structure of antennal sensilla of the female sphinx moth, *Manduca sexta* (Lepidoptera: Sphingidae).: I.: Trichoid and basiconic sensilla. Canadian Journal of Zoology-Revue Canadienne De Zoologie *77*, 290-301.
35. Shields, V.D.C., and Hildebrand, J.G. (1999). Fine structure of antennal sensilla of the female sphinx moth, *Manduca sexta* (Lepidoptera: Sphingidae).: II.: Auriculate, coeloconic, and styliform complex sensilla. Canadian Journal of Zoology *77*, 302-313.
36. Palaoro, A.V., Gole, A.R., Sun, Y.M., Puchalski, A., Beard, C.E., Adler, P.H., and Kornev, K.G. (2023). Wettability and morphology of proboscises interweave with hawkmoth evolutionary history. Journal of Experimental Biology *226*.
37. Landau, L.D., and Lifshitz, E.M. (1986). Theory of Elasticity, Volume 7, 3 Edition, (Reed Educational and Professional Publishing Ltd.).
38. Kiusalaas, J. (2015). Numerical methods in engineering with Matlab, 3rd edition Edition, (Cambridge University Press).
39. Donley, G., Sun, Y.M., Pass, G., Adler, P.H., Beard, C.E., Owens, J., and Kornev, K.G. (2022). Insect antennae: Coupling blood pressure with cuticle deformation to control movement. Acta Biomater. *147*, 102-119.
40. Chapman, R.F. (2013). The Insects: Structure and Function.
41. Goldstein, P.Z. (2017). Diversity and significance of Lepidoptera: a phylogenetic perspective. In Insect Biodiversity: Science and Society, Volume I, 2nd edition Edition, R.G. Foottit and P.H. Adler, eds. (Chichester, UK: Wiley-Blackwell), pp. 463-495.

42. Lees, D.C., and Zilli, A. (2019). Moths. A complete guide to biology and behavior, (Washington DC: Smithsonian books).
43. Hildebrand, J.G. (1996). Olfactory control of behavior in moths: Central processing of odor information and the functional significance of olfactory glomeruli. Journal of Comparative Physiology a-Neuroethology Sensory Neural and Behavioral Physiology *178*, 5-19.
44. Sane, S.P. (2016). Neurobiology and biomechanics of flight in miniature insects. Current Opinion in Neurobiology *41*, 158-166.
45. Sant, H.H., and Sane, S.P. (2018). The mechanosensory-motor apparatus of antennae in the Oleander hawk moth (Daphnis nerii, Lepidoptera). Journal of Comparative Neurology *526*, 2215-2230.
46. Taha, H.E., Kiani, M., Hedrick, T.L., and Greeter, J.S.M. (2020). Vibrational control: A hidden stabilization mechanism in insect flight. Science Robotics *5*.
47. Hearn, E.J. (1997). Mechanics of materials, Volume 1, 3rd Edition, (Boston: Butterworth Heinemann).
48. Vogel, S. (1996). Life in Moving Fluids: The Physical Biology of Flow, (Princeton, NJ: Princeton University Press).
49. Fung, Y.C. (2008). An Introduction to the Theory of Aeroelasticity, (New York: Dover Publications).
50. Kraus, J.D. (1988). Antennas, 2nd Edition, (New York: McGraw-Hill College; Subsequent edition).
51. Johnson, T.L., Elgar, M.A., and Symonds, M.R.E. (2022). Movement and olfactory signals: Sexually dimorphic antennae and female flightlessness in moths. Front. Ecol. Evol. *10*.
52. Smith, G.P., Davidowitz, G., Alarcón, R., Papaj, D.R., and Bronstein, J.L. (2022). Sex differences in the foraging behavior of a generalist hawkmoth. Insect Science *29*, 304-314.
53. de Camargo, W.R.F., de Camargo, N.F., Correa, D.D.V., de Camargo, A.J.A., and Diniz, I.R. (2015). Sexual Dimorphism and Allometric Effects Associated With the Wing Shape of Seven Moth Species of Sphingidae (Lepidoptera: Bombycoidea). Journal of Insect Science *15*.
54. Elgar, M.A., Johnson, T.L., and Symonds, M.R.E. (2019). Sexual selection and organs of sense: Darwin's neglected insight. Animal Biology *69*, 63-82.
55. Richards, O.W., and Davies, R.G. (1977). Imms' general textbook of entomology, Volume Vol. 1: Structure, physiology and development., 10th Edition, (New York: Halsted Press).
56. Stevenson, R.D., Corbo, K., Baca, L.B., and Le, Q.D. (1995). Cage size and flight speed of the Tobacco hawkmoth *Manducs sexta*. Journal of Experimental Biology *198*, 1665-1672.
57. Aiello, B.R., Bin Sikandar, U., Minoguchi, H., Bhinderwala, B., Hamilton, C.A., Kawahara, A.Y., and Sponberg, S. (2021). The evolution of two distinct strategies of moth flight. Journal of the Royal Society Interface *18*.
58. Matthews, M., and Sponberg, S. (2018). Hawkmoth flight in the unsteady wakes of flowers. Journal of Experimental Biology *221*.
59. Hongu, T., Phillips, G.O., and Takigami, M. (2005). New millenium fibers, (Cambridge, England: Woodhead Publishing Ltd).

Flexural rigidity of hawkmoth antennae depends on the bending direction

Adam Puchalski[1], Zoë McCarthy[1], Alexandre Varaschin Palaoro[1], Arthur A. Salamatin[1], Agnes Nagy-Mehesz[2], Guzeliya Korneva[2], Charles E. Beard[3], Jeffery Owens[4], Peter H. Adler[3] and Konstantin G. Kornev[1]

[1]Department of Materials Science and Engineering, Clemson University, Clemson, South Carolina, USA, 29634. E-mail: kkornev@clemson.edu

[2]Department of Plant and Environmental Sciences, Clemson University, Clemson, South Carolina USA, 29634

[3]Air Force Civil Engineer Center, Tyndall Air Force Base, Florida

Supplementary Material.

Table S1. Summary of experimental conditions during which MicroTensile Testing was conducted on hawkmoth antennae.

Sample #	Experiment Date	Temp (C)	Humidity (%)	Sex	Capture Date	Emergence Date
Manduca sexta						
33	9/14/2022	26	56	M	n/a	9/5/22
10						
22	8/12/2022	22	70	M	n/a	n/a
21	8/12/2022	22	70	M	n/a	n/a
34	10/12/2022	24	54	F	10/10/2022	n/a
35	10/14/2022	23	38	M	10/7/2022	n/a
36	10/14/2022	23	38	M	10/7/2022	n/a
37	10/19/2022	23	20	F	10/7/2022	n/a
38	10/21/2022	23	25	F	10/10/2022	n/a
39	10/21/2022	23	25	F	10/10/2022	n/a
40	10/21/2022	23	25	F	n/a	10/7/2022

42	11/30/2022	23	51	F	n/a	11/22/2022
43	11/30/2022	23	51	F	n/a	11/22/2022
Ceratomia catalpae						
22	7/29/2022	22	73	M	7/24/2022	n/a
20	8/1/2022	22	72	M	7/24/2022	n/a
21	8/1/2022	23	68	F	7/28/2022	n/a
24	8/2/2022	22	70	M	7/28/2022	n/a
Xylophanes tersa						
1	9/7/2022	23	66	M	9/1/2022	n/a
2	9/7/2022	23	66	M	9/1/2022	n/a
3	9/7/2022	23	66	M	9/1/2022	n/a
Manduca quinquemaculata						
1	9/7/2022	23	56	M	9/14/2022	n/a
2	9/7/2022	23	56	M	9/14/2022	n/a
3	9/7/2022	23	58	M	9/14/2022	n/a

Shooting method.

The Euler elastica equations are:

$$f\,\frac{d}{ds}\left(\frac{d\psi}{ds}\right) - W\sin\psi = 0,\ dx/ds = \sin\psi,\ dy/ds = \cos\psi \qquad \text{(S1)}$$

We rewrite eqs.(S1) as a system of four dimensionless 1st order differential equations by introducing $s = LS, x = LX, y = LY, \tau = WL^2/f$:

$$\left(\frac{d\psi}{dS}\right) = v, \quad \frac{dv}{dS} = \tau \sin\psi, \quad dX/\mathrm{dS}=\sin\psi, \quad d\mathrm{Y}/\mathrm{dS}=\cos\psi. \tag{S2}$$

With the four equations, three initial conditions are known.

$$\psi(0) = \frac{\pi}{2}, X(0) = 0, Y(0) = 0 \tag{S3}$$

And one condition is unknown; we set $\frac{d\psi}{dS}(0) = u$ where u is an arbitrary parameter which must be obtained by integrating (S2)-(S3) until the condition $\frac{d\psi}{dS}(1) = 0$ is satisfied. The equations are solved using the ODE45 function provided in MATLAB, and this is run through every iteration of the loop until the last value $\frac{d\psi}{dS}(1) = 10^{-5}$ for the curvature is reached.

To ensure that the experimental X-values line up with the values from the shooting method, the numerical data were interpolated to provide a continuous function. Linear interpolation involves estimating intermediate values between the two known data points using a straight line. This allowed for smoother transitions, more accurate representation of data, and a more accurate method of comparing the two data sets. As seen in Figure S1, the interpolated data have the same trend to the original data from the shooting method.

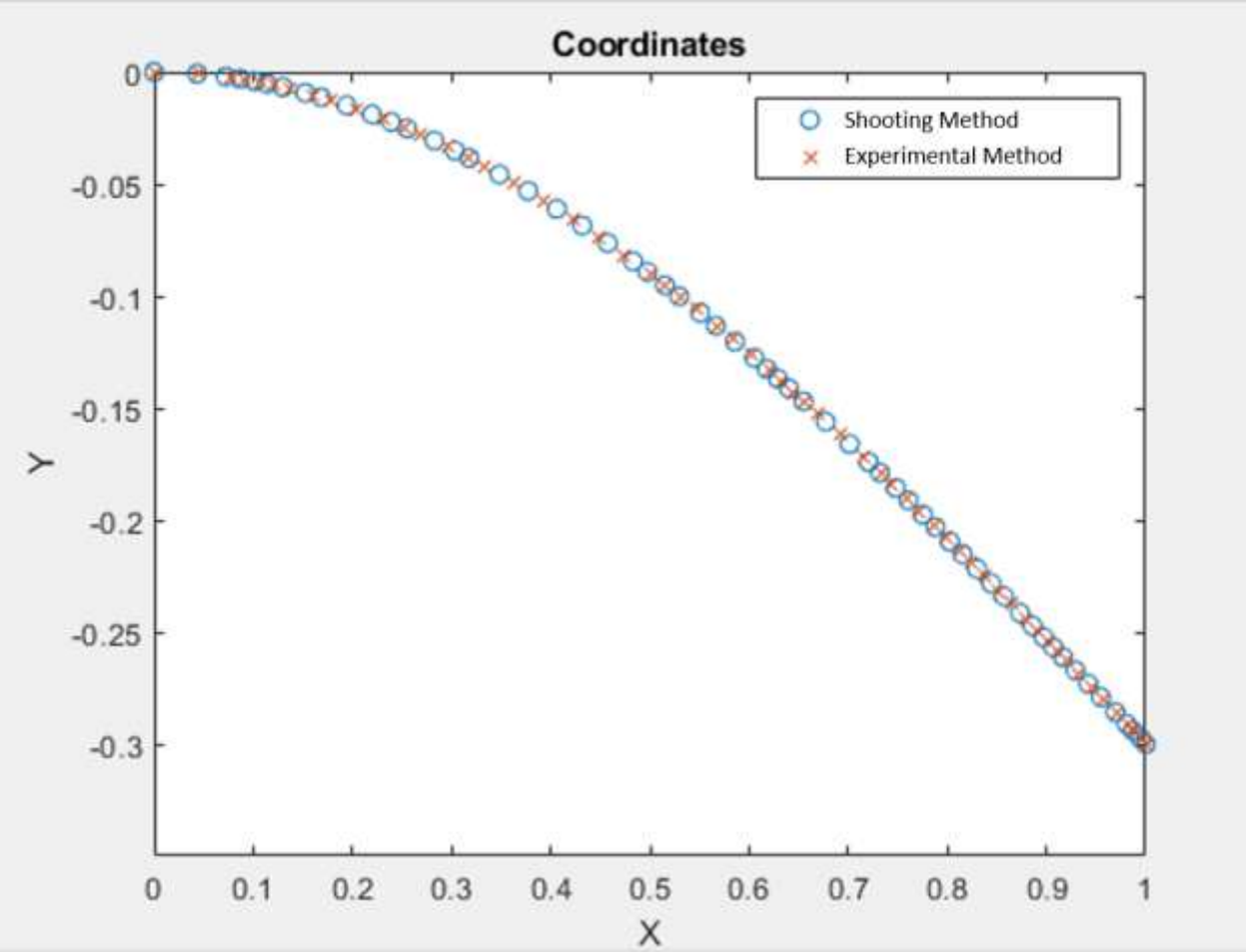

Figure S1: *A plot of the shooting method coordinates before and after interpolation.*

Calibration with the Polynomial Solution

To verify that the shooting method is working correctly, a polynomial solution is derived and compared to the results of the shooting method. Introducing the inclination angle δ as $\psi = \frac{\pi}{2} - \delta$ and considering small deflections, $\delta \ll 1$, we have

$$\sin \psi = \sin\left(\frac{\pi}{2} - \delta\right) = \cos\delta \approx 1 \cos \psi = \cos\left(\frac{\pi}{2} - \delta\right) = \sin\delta \approx \delta, \quad \text{(S4)}$$

Substituting eqs.(S4) in eqs.(S2), we have dY/dS ≈ dY/dX≈ δ . Therefore,

$$\frac{d^3Y}{dX^3} + \tau = 0 \quad \text{(S5)}$$

Equation (S5) was integrated three times:

$$\int[\frac{d^3Y}{dX^3} + \tau = 0] => -\tau X + a,$$

$$\int [-\tau X + a]dX => -\tau \frac{X^2}{2} + aX + b,$$

$$\int [\tau \frac{X^2}{2} + aX + b\,]\,dX => Y = -\tau \frac{X^3}{6} + a\frac{X^2}{2} + bX + c.$$

(S6)

Using the boundary condition $Y(0) = 0 => c = 0$ and the second boundary condition $dY/dX(0) = 0 => b = 0$ Finally, the remaining boundary condition $\frac{d^2Y}{dX^2}(1) = 0$ gives $a = \tau$. Thus, we have

$$Y = -\tau \frac{X^3}{6} + \tau \frac{X^2}{2} \quad \text{(S7)}$$

Figure S2 shows the results of numerical solution and eq.(S7) for τ = 0.1.

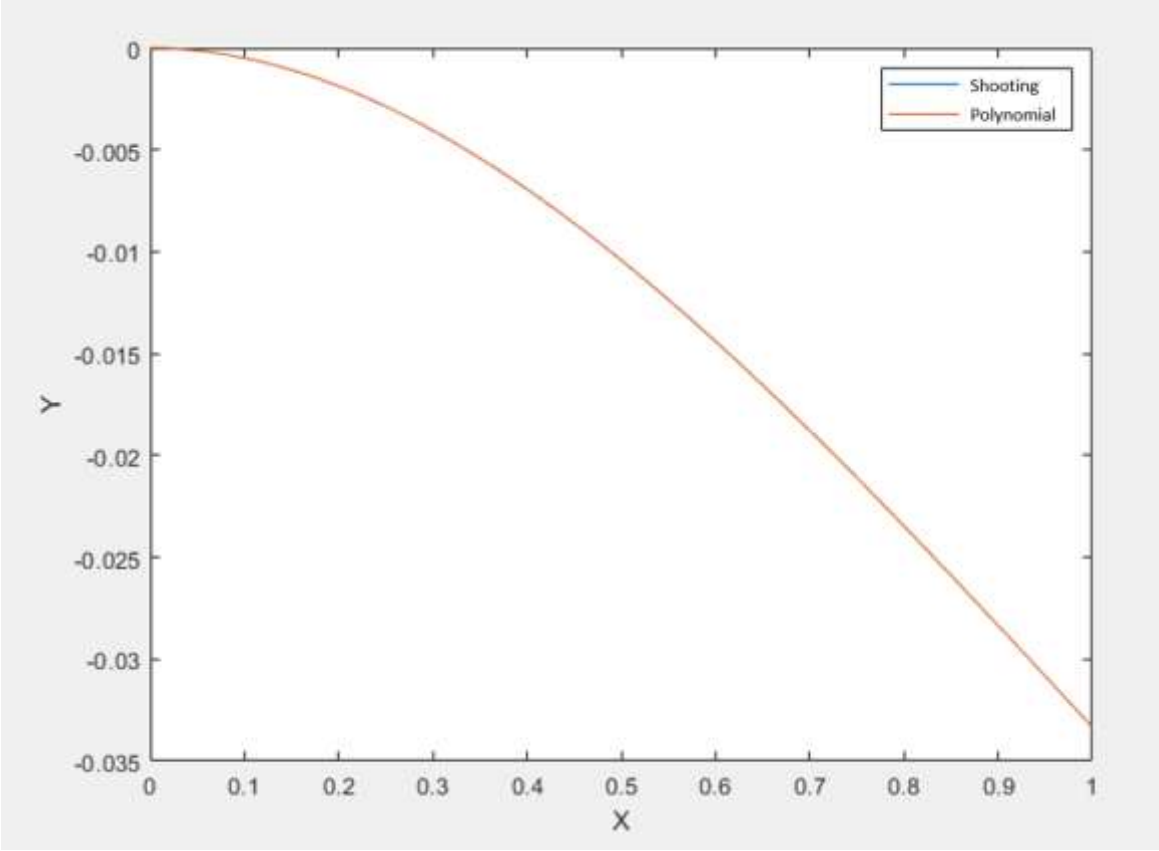

Figure S2: *A plot Y as a function of X obtained by the shooting method and by the polynomial solution (S6)*

The two functions are so similar that they overlap. This confirms that the shooting method does an adequate job of solving the Euler elastica.

The goodness of fit

The goodness of fit was measured by the following equation:

$$f = \sum_{i=1}^{n}[(X(s) - \hat{X}(s))^2 - (Y(s) - \hat{Y}(s))^2] \quad \text{(S8)}$$

where X and Y are the values of the actual data, and $\hat{X}$ *and* $\hat{Y}$ are the values from the shooting method for each node *i*. For each tau-value in the Euler elastica, we have a single f-value, eq.(38), representing the error of the given fit. This error in this case, f, for each tau value was plotted in Figure S3. The Tau output with the lowest error value was chosen as the 'best fit' and then was further analyzed in a tighter numerical region to obtain higher accuracy.

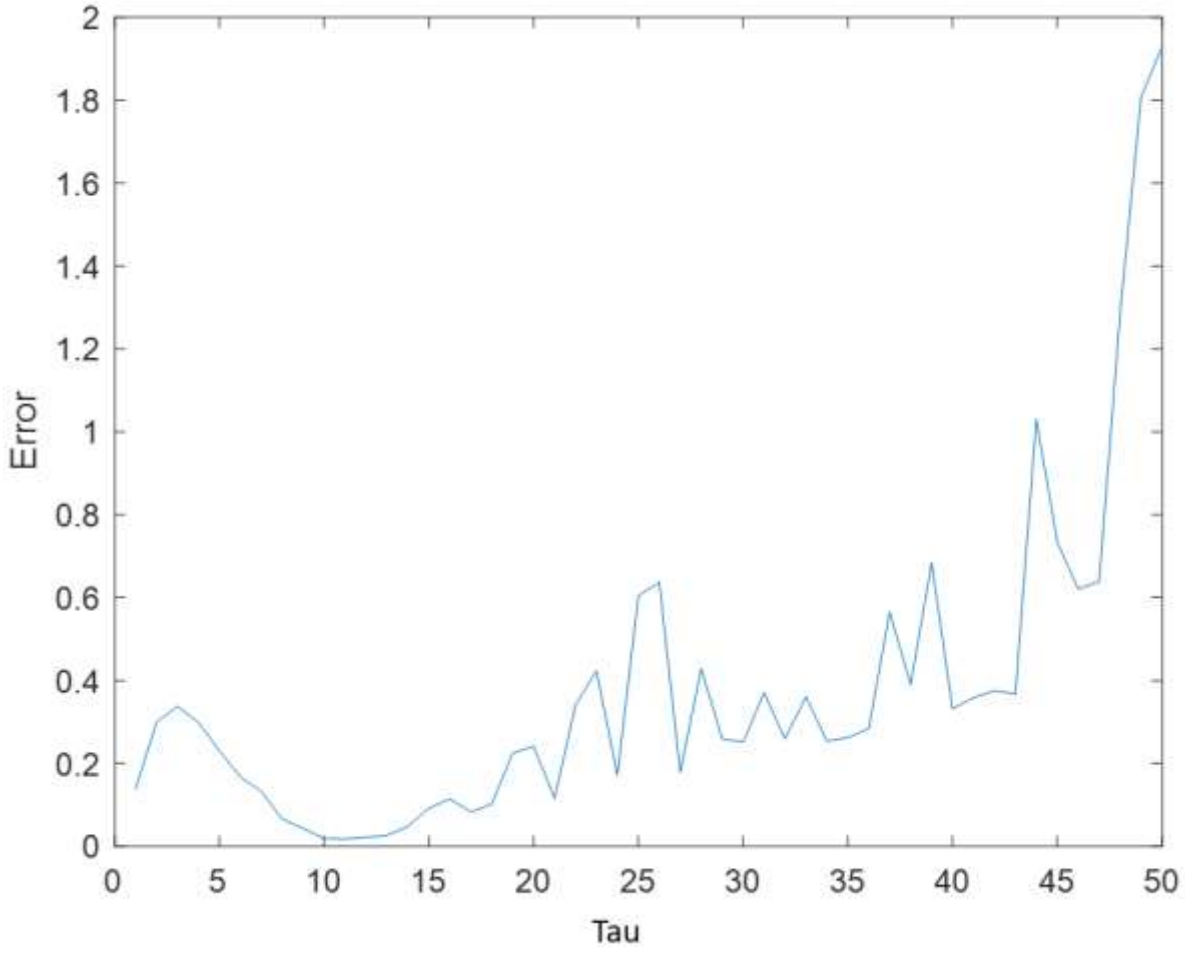

Figure S3: *A plot of the fitting error, function f, as a function of tau obtained by the shooting method for various tau values, where error is measured by (S7).*

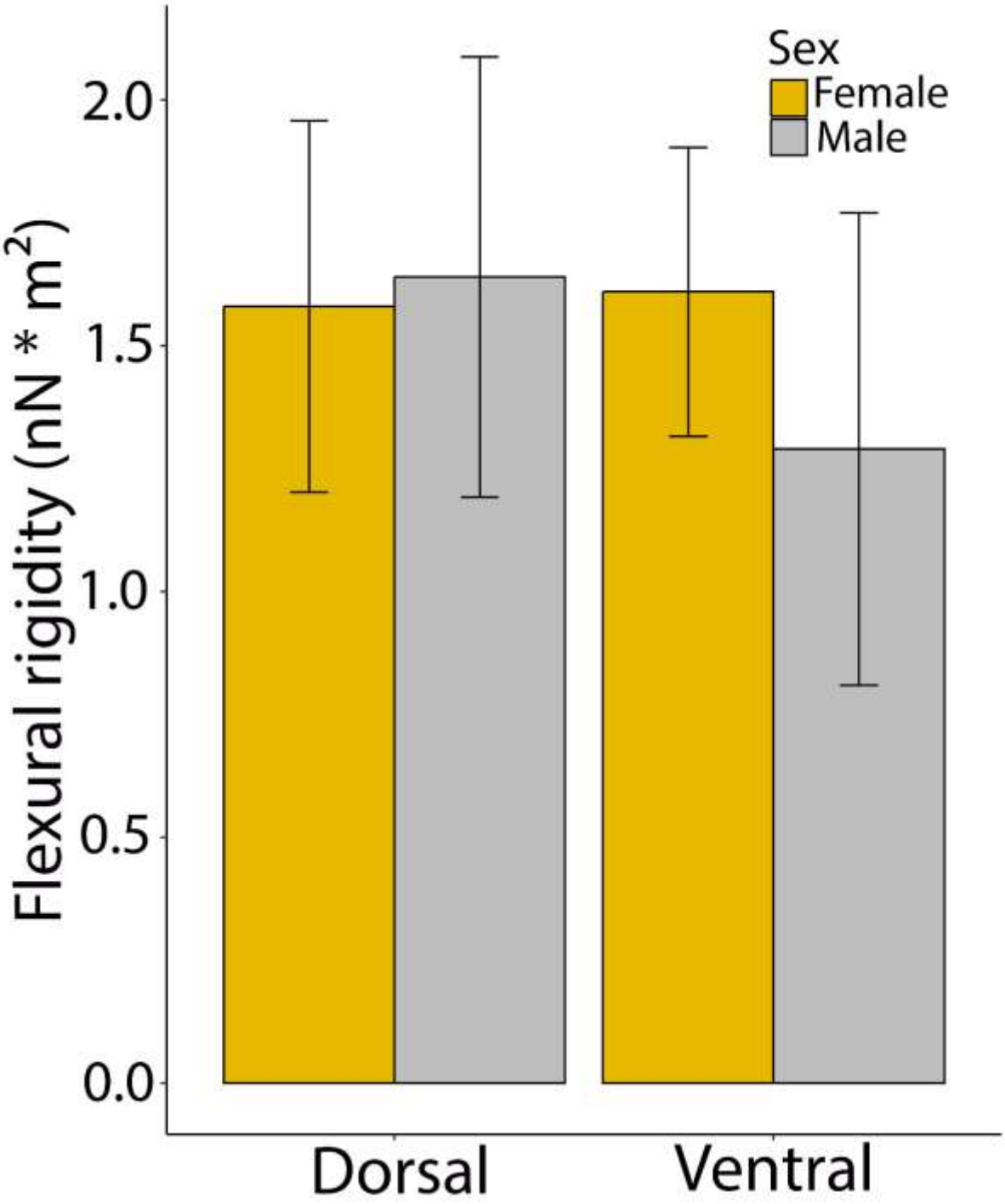

Figure S4: *Data on the sidewise bending of the antennae of M. sexta. The "dorsal" bars specify experiments with the camera facing the dorsal side of the antennae, and the "ventral" bars specify experiments with the camera facing the ventral side.*